Article

Cryogenic X-ray photoelectron spectroscopy for battery interfaces

https://doi.org/10.1038/s41586-025-09618-3

Received: 31 December 2024

Accepted: 11 September 2025

Published online: 22 October 2025

Check for updates

Sanzeeda Baig Shuchi[1], Giulio D'Acunto[1], Philaphon Sayavong[2], Solomon T. Oyakhire[1,7], Kenzie M. Sanroman Gutierrez[1], Juliet Risner-Jamtgaard[3], Il Rok Choi[4], Yi Cui[4,5,6]✉ & Stacey F. Bent[1,6]✉

Understanding the chemical environment of pristine interfaces is a long-sought goal in electrochemistry, materials science and surface science. A substantial understanding of one such interface, the solid electrolyte interphase (SEI) in lithium anodes, originates from X-ray photoelectron spectroscopy (XPS)[1,2]. However, room temperature (RT) combined with ultrahigh vacuum (UHV) can induce major SEI evolution from reactions and volatilization during XPS[1,2]. Thus, a technique is necessary for SEI stabilization. Here we develop cryogenic (cryo)-XPS with immediate plunge freezing and demonstrate SEI preservation. We discover substantially different SEI speciation and a thicker pristine SEI with cryo-XPS, free from RT-associated thickness reduction and alterations to important species, including LiF and Li_2O, in UHV. This new access to pristine SEI composition enables performance correlations across diverse electrolyte chemistries. Primarily, we highlight the necessity of studying sensitive interfaces under cryogenic conditions.

Electrode-electrolyte interfaces are crucial for constructing high-performing electrochemical devices[3–5]. A notable example is the solid electrolyte interphase (SEI) in lithium (Li) batteries, which is defined as the nanometre-thick passivation layer formed at the anode–electrolyte interface from electrolyte decomposition[6,7]. SEI is considered the most important solid interphase in Li-ion and Li metal batteries[6,8].

X-ray photoelectron spectroscopy (XPS) is the main technique for SEI chemical characterization because of its specific molecular species identification capability and nanoscale depth sensitivity, contributing to most of our understanding of the SEI chemical environment[1,2]. However, SEI characterization with XPS is predominantly performed at room temperature (RT). At RT, spontaneous decomposition and growth reactions can alter SEI composition[1,9–13]. Moreover, the ultrahigh vacuum (UHV) conditions of the XPS chamber ($\lesssim 10^{-6}$ Pa) can reduce SEI thickness at RT through volatilization of SEI species and decomposition products[1]. Moreover, beam damage to the SEI often occurs during X-ray and transmission electron microscopy (TEM) analyses[12,14]. Consequently, RT-XPS may not reflect what is truly at the interphase but rather depict an evolved interphase.

Here, we develop cryogenic (cryo)-XPS transfer (Fig. 1 and Methods) by performing plunge freezing of the SEI sample instantly in liquid N_2 (LN_2, about −196 °C) to preserve the SEI in its pristine chemical state. We propose that cryo-XPS can create valuable impacts to understand the detailed chemical environment of pristine SEI because cryogenic conditions can halt chemical reactions and freeze UHV-volatile species. Most chemical reactions are halted because of slow reaction kinetics at cryogenic temperature (cryoT)[12,15]. We propose that the true SEI thickness can also be retained, benefiting from the lower vapour pressure of different frozen SEI species at cryoT. This is reasonable as we draw inspiration from cryo-electron microscopy (cryo-EM), in which cryogenic conditions have led to important discoveries on preserved interfaces in batteries[12,15–18] and in biology[19–25]. Particularly, cryo-XPS can be highly impactful and complementary to cryo-EM for SEI characterization because it can offer information on detailed chemical speciation, including different oxidation states. We perform spectra collection at around −110 °C (the minimum allowed temperature for our cryogenic sample holder), so the sample eventually warms up to about −110 °C, which we find to be sufficient to preserve the sample during analysis. We confirm the SEI thickness preservation from Li 1*s* high-resolution spectra.

Time-dependent SEI preservation and evolution

To understand the time-dependent SEI compositional changes during cryo-XPS and RT-XPS, we compare the time-resolved XPS data collected from the same analysis spot using a plunge frozen SEI sample with cryo-XPS and again after heating it to RT (Fig. 2). First, we notice that the high-resolution XPS spectra for the F 1*s*, O 1*s* and N 1*s* peaks collected under cryo-XPS and UHV conditions remain similar as time passes (0 min and after 60 min). By contrast, after heating the sample to RT, major changes are observed when analysing the same spot. After 60 min at RT, the composition of the same spot changes even further. This result is crucial and establishes the preservation effect of cryo-XPS and the sample evolution effect of RT-XPS. Discussing the specific example for F 1*s*, increases in the intensity of the peak associated with LiF (around 684.5 eV) are observed both on reaching RT and after 60 min at RT. Since species amount scales with peak intensity, the results suggest that cryo-XPS shows a relatively lower LiF amount and a time-invariant

[1]Department of Chemical Engineering, Stanford University, Stanford, CA, USA. [2]Department of Chemistry, Stanford University, Stanford, CA, USA. [3]Stanford Nano Shared Facilities, Stanford University, Stanford, CA, USA. [4]Department of Materials Science and Engineering, Stanford University, Stanford, CA, USA. [5]Stanford Institute for Materials Energy and Energy Sciences, SLAC National Laboratory, Menlo Park, CA, USA. [6]Department of Energy Science and Engineering, Stanford University, Stanford, CA, USA. [7]Present address: Department of Materials Science and Engineering, University of California Berkeley, Berkeley, CA, USA. ✉e-mail: yicui@stanford.edu; sbent@stanford.edu

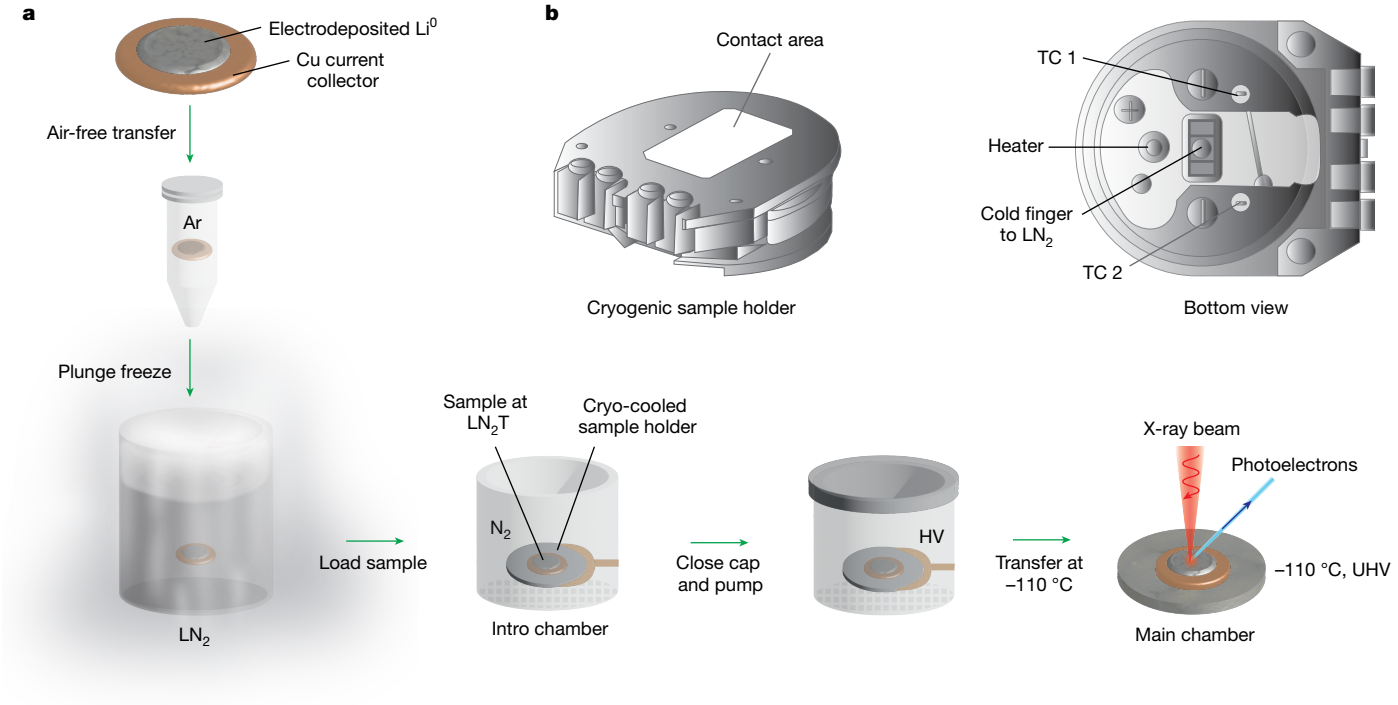

Fig. 1 | Cryo-XPS transfer process for SEI preservation. a, Li metal is electrodeposited on a Cu current collector and then plunged into LN_2 immediately after sample preparation. The sample at LN_2T is then placed onto the contact area of a cryo-cooled sample holder. The N_2 pressure, higher than ambient pressure, inside the intro chamber ensures an inert environment around the sample right before pumping. Transfer to the main chamber and spectra collection are performed at about −110 °C. **b**, The cryogenic sample holder is cooled using the cold finger crimped to a Cu wire blade that leads to an LN_2 dewar. LN_2, liquid nitrogen; HV, high vacuum; UHV, ultrahigh vacuum; TC, thermocouple.

SEI composition. The relative LiF content increases once the SEI reaches RT. After an elongated stay at RT, the relative LiF content rises even further. Analogous preservation and evolution effects are observed for all the other SEI constituents, including inorganic species such as Li_2O and Li_3N in O 1*s* and N 1*s* regions, respectively (Fig. 2 and Extended Data Figs. 1 and 2). A more pronounced effect is observed during RT-XPS of an unwashed SEI sample as it retains a larger quantity of reactive and volatile species from the electrolyte (Extended Data Fig. 3). Additional cryo-XPS data are shown in Supplementary Fig. 1. Speciation comparison between our cryo-XPS data with selected available literature RT-XPS data on 1 M LiFSI/DME SEI is shown in Supplementary Table 1.

We further investigate the necessity of immediate plunge freezing and the reversibility of SEI evolution at RT by re-cooling the SEI to cryoT (Extended Data Fig. 4). The relative LiF content in the F 1*s* peak increases from cryo-XPS both after heating to RT and again after re-cooling sequentially. This result indicates that composition evolution at RT is irreversible, and gradual cooling under vacuum does not preserve the SEI composition. Thus, subjecting the sample to plunge freezing in liquid N_2 immediately after sample preparation is recommended. Furthermore, we also consider possibilities of side reactions between nitrogen and lithium in LN_2 or in the XPS intro chamber (Supplementary Note 1 and Supplementary Fig. 2) and residual gas altering surface composition (Supplementary Note 2), which are found to be minor.

Reaction effect

We study the reaction effect by comparing the SEI chemical composition under three experimental conditions, namely, cryo-XPS, in situ heating of the same sample to RT and regular RT-XPS (Fig. 3a), each in a high-performing localized high-concentration electrolyte (LHCE). We consider F 1*s* and O 1*s* spectral regions due to LiF (refs. 26–28) and Li_2O (refs. 29,30) often discussed as beneficial SEI species for improved cycling. Analogous to our previous observations from the F 1*s* peaks (Fig. 2 and Extended Data Figs. 2–4), we find that both cryo-heated to RT-XPS and regular RT-XPS yield a higher LiF peak intensity than cryo-XPS (F 1*s* region; Fig. 3a). Therefore, it is concluded that performing RT-XPS analysis on the SEI leads to an overestimation of the amount of LiF in the SEI. This overestimation is misleading because higher LiF content is often associated with improved cycling performance[26–28]. The higher LiF peak intensity in the SEI at RT can be explained by several reactions and volatilization resulting in stable LiF as the remaining product (Supplementary Note 3). A possible reaction for this model SEI from LHCE leading to a stable LiF end product can progress by S–F bond cleavage of SO_xF_y species[2] written as,

$$\mathrm{LiN(SO_2F)_2\ (LiFSI\ salt) \rightarrow LiF(stable\ solid) + SO_2}$$
$$\mathrm{-NSO_2F(further\ decomposition,\ volatilization)}$$

The reaction effect for the SEI on Li can be explained by simultaneous SEI decomposition forming more stable products and SEI growth reactions from chemical corrosion of Li (refs. 1,9–13). We clarify that SO_xF_y is the general formula inclusive of both the LiFSI salt ($LiNS_2F_2O_4$) and the SEI products formed from its decomposition. SEI decomposition reactions are more favourable than SEI growth atop a more noble Cu substrate in the absence of electrodeposited Li (ref. 31). However, even on Cu, we observe a drastic change in SEI composition between cryogenic and RT conditions towards higher LiF at RT (Extended Data Fig. 5), suggesting that SEI decomposition reactions may be the primary cause of composition evolution.

Next, we consider the presence of a noticeable Li_2O peak under cryogenic conditions that is absent under RT conditions in the O 1*s* spectral region (Fig. 3a). Because Li_2O has extremely low vapour pressure and is not reported to volatilize in vacuum even at 1,000 °C (refs. 32,33), the absence of Li_2O during RT-XPS can be justified through reaction effects (Supplementary Note 4). The relative presence of Li_2O is reversed at cryoT and RT for the SEI in a low-performing carbonate electrolyte,

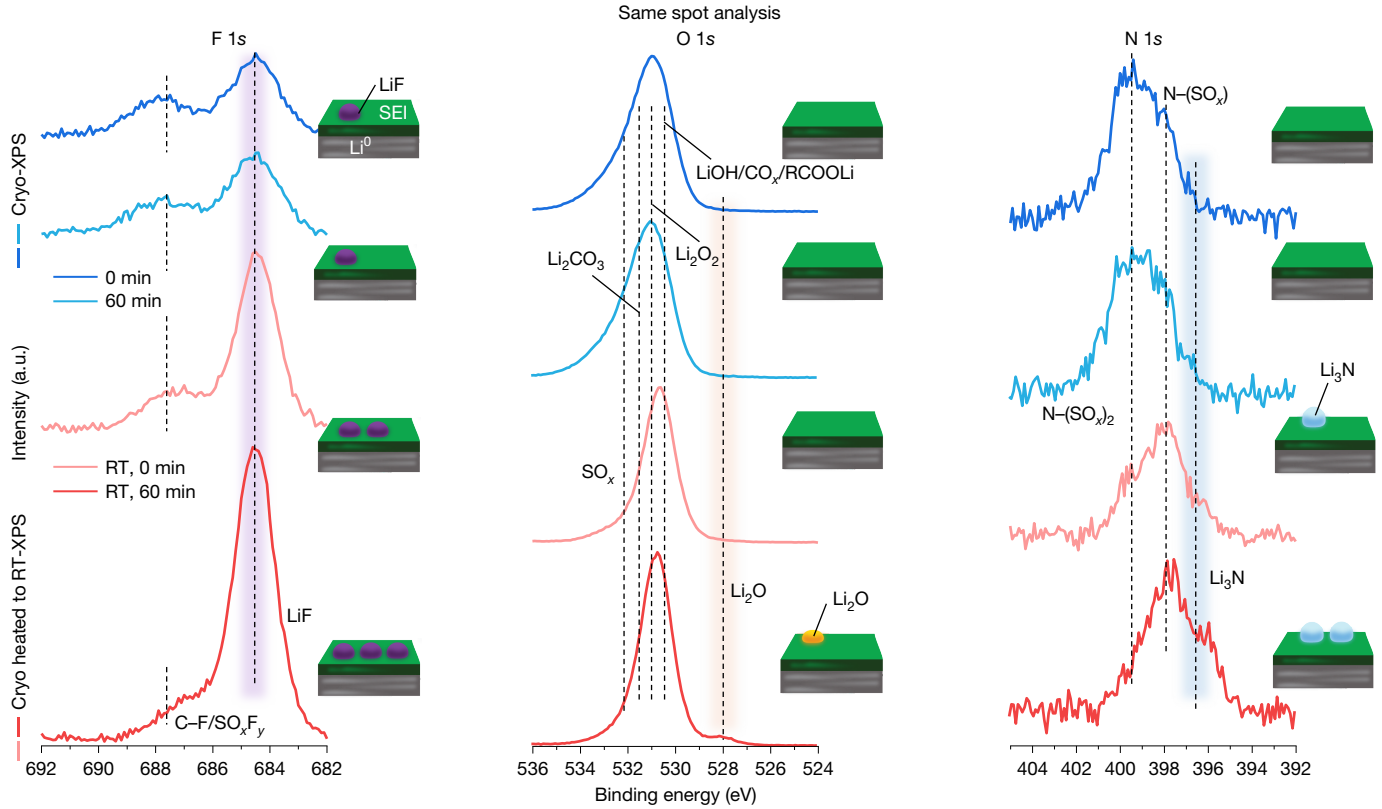

Fig. 2 | Time-dependent SEI preservation and evolution. Time-resolved high-resolution spectra for F 1*s*, O 1*s* and N 1*s* peaks with cryo-XPS and cryo-heated to RT-XPS with schematics showing the evolution of LiF, Li_2O and Li_3N species at 0 min and at 60 min. The measurements are carried out on one sample at the same spot to capture the SEI evolution decoupled from SEI spatial heterogeneities. The electrolyte used is 1 M LiFSI/DME. Spectra are normalized with respect to the SO_xF_y/C–F peak.

1 M $LiPF_6$/EC-DEC (LP), which could be due to favourable Li_2O formation reactions (Extended Data Fig. 6 and Supplementary Note 4). Li_2O is prevalent in the SEI from high coulombic efficiency (CE) electrolytes[29] and is shown to improve anodic stability[30]. Indeed, the Li_2O content in the SEI correctly correlates with the CE trend of LHCE and carbonate electrolyte under cryo-XPS conditions. By contrast, the evolved SEI measured with RT-XPS fails to provide the relevant performance associations due to spontaneous reactions resulting in deviations from the pristine SEI. High-performing LHCE electrolyte and low-performing LP electrolyte are discussed to better correlate SEI speciation with performance. Li_3N-associated reactions are added in Supplementary Note 5.

UHV effect

We explain the UHV effect from the observation of the underlying Li^0 metal peak beneath the SEI. Although only a broad SEI-associated Li 1*s* peak is observed with cryo-XPS, the metallic Li^0 peak appears during RT and cryo-heated to RT analyses (Li 1*s* region; Fig. 3b). The results indicate that a thinning of the SEI occurs at RT under UHV which can trigger volatile species to leave the surface (Fig. 3c). The SEI thickness can be estimated from the photoelectron escape depth from Li^0 metal[34] (about 4.2 nm ± 20%; Supplementary Note 6). The observation of a Li^0 metal peak suggests that the SEI thickness is less than $\lesssim$4.2 nm ± 20% at RT, whereas the SEI thickness is >4.2 nm ± 20% at cryoT[35]. This estimated SEI thickness from cryo-XPS is consistent with that from cryo-TEM measurements reported to be ≥7.7 nm for the model LP electrolyte SEI[15] (Extended Data Fig. 7a,b). This result has implications for RT-XPS measurements as the SEI thickness shows a marked reduction at RT and a high deviation from the true SEI thickness. Here, a specific case of the SEI formed with LP electrolyte is shown because it displays distinguishable Li^0 metal peaks at RT. Furthermore, our cryo-XPS findings compare favourably with cryo-scanning TEM electron energy loss spectroscopy (cryo-STEM EELS) data, with both demonstrating higher contribution from C=O bond from C 1*s* (XPS) and C K edge (EELS), respectively, for LP-SEI, whereas the C=O contribution is lower for RT-XPS[15] (Extended Data Fig. 7c–e).

Apart from giving information on SEI thickness, Li 1*s* spectra can explain the relative diversity among different SEI species. Because most SEI species are bonded with Li, a higher full-width half maximum (FWHM) of SEI-associated Li 1*s* peaks can be translated to having an SEI formed by several different species bonded to Li. By contrast, a lower FWHM suggests a more homogeneous SEI composition. A higher Li 1*s* FWHM is observed for LHCE-SEI at cryoT compared with RT conditions (Extended Data Fig. 8), indicating that the SEI is more heterogeneous at its pristine state during cryo-XPS, whereas only non-volatile species and stable reaction end products dominate the SEI composition at RT. This interpretation is also supported by Extended Data Fig. 9 and Supplementary Fig. 3, which show a higher degree of atomic concentration change with sputtering during cryo-XPS than cryo-heated to RT-XPS, probably because both stable and unstable SEI species are preserved during cryo-XPS. In all the cases observed, the results indicate that we can capture only an evolved SEI with RT-XPS due to reaction and UHV effects (Fig. 3c).

Beam effect

To show the beam damage effect, we collect five consecutive spectra at cryoT (Fig. 3d) and RT (Fig. 3e). The change between the consecutive spectra is a relative measure of the beam damage effect. First, we observe only a slight increase in LiF intensity after five consecutive X-ray beam exposures for both cryo-XPS and RT-XPS spectra (Fig. 3d,e). This result indicates that the composition change due to the beam damage

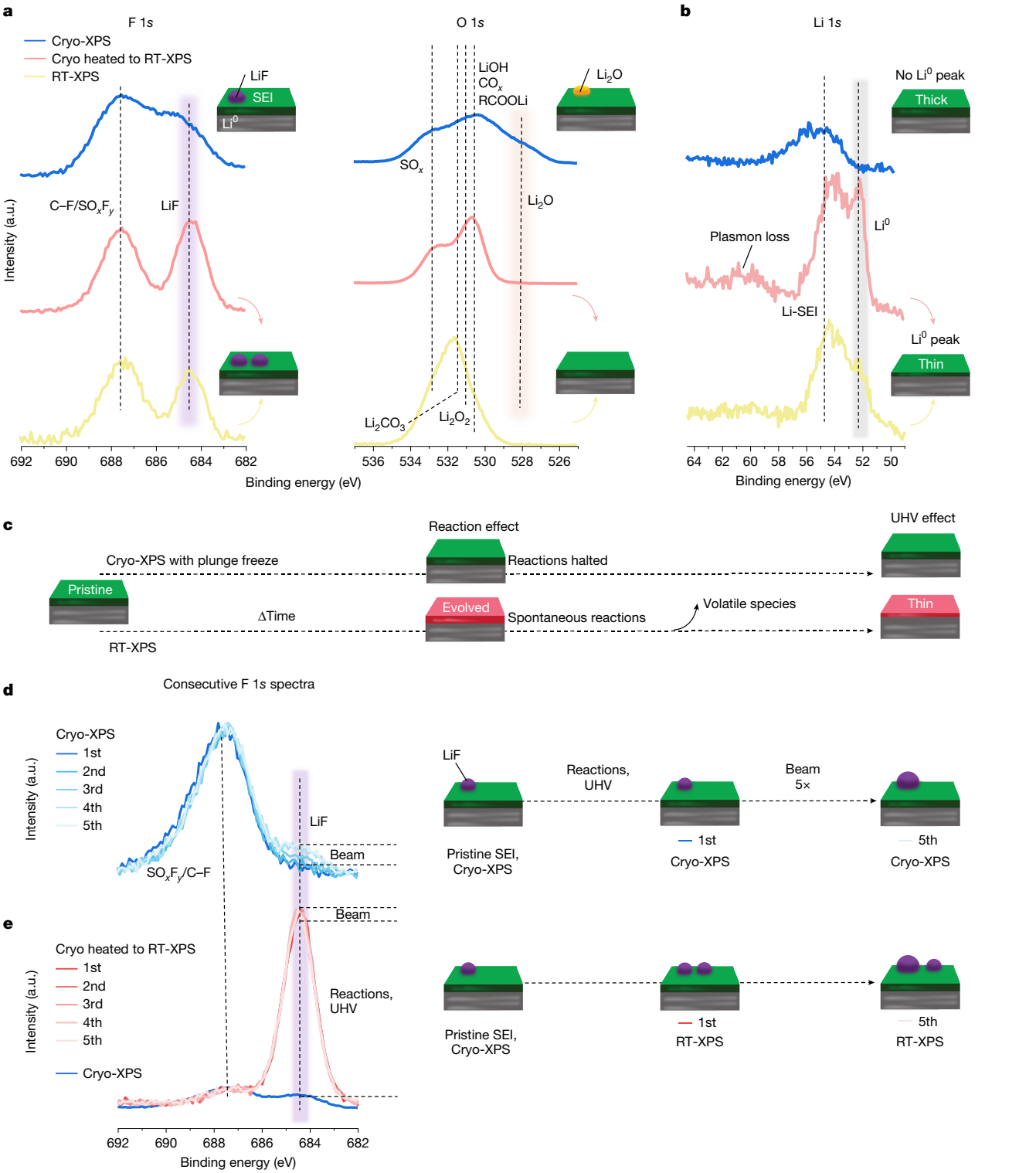

Fig. 3 | Reaction, UHV and X-ray beam effects on SEI chemical composition. **a**,**b**, High-resolution spectra for F 1*s* peaks, O 1*s* peaks (**a**), and Li 1*s* peaks (**b**) collected using cryo-XPS (blue, top), cryo-heated to RT-XPS (pink, middle) and RT-XPS (yellow, bottom) with schematics showing SEI evolution. **c**, Schematics showing reaction and UHV effects for cryo-XPS and RT-XPS over time. The measurements shown in **a** for F 1*s* and O*s* are carried out using LiFSI-1.2 DME-3 TTE by molar ratio (LHCE) electrolyte. The measurements shown in **b** for Li 1*s* are taken using 1 M $LiPF_6$/EC-DEC (LP) electrolyte. Global normalization is performed with respect to the C–F peak in F 1*s* high-resolution spectra for the same electrolyte as shown in **a** and Extended Data Fig. 6a. **d**,**e**, X-ray beam effect during consecutive spectra collection. Five consecutive high-resolution spectra for F 1*s* peak with cryo-XPS (**d**), cryo-heated to RT-XPS (**e**). The spectra are collected from the same sample to avoid sample preparation differences. Spectra shown in **e** are collected from a different position than **d** to avoid the damaged spot. The consecutive spectra are compared with corresponding cryo-XPS spectra from the same spot, and schematics showing the effects are added. Sufficient time is allowed after heating (about 2 h) to avoid time-dependent evolution effects demonstrated in Fig. 2. The data are normalized with respect to the C–F/SO_xF_y peak. The measurements are carried out using 4 M LiFSI/DME electrolyte. For X-ray beam effect experiments, each F 1*s* spectrum collection takes about 1.5 min with the set parameters.

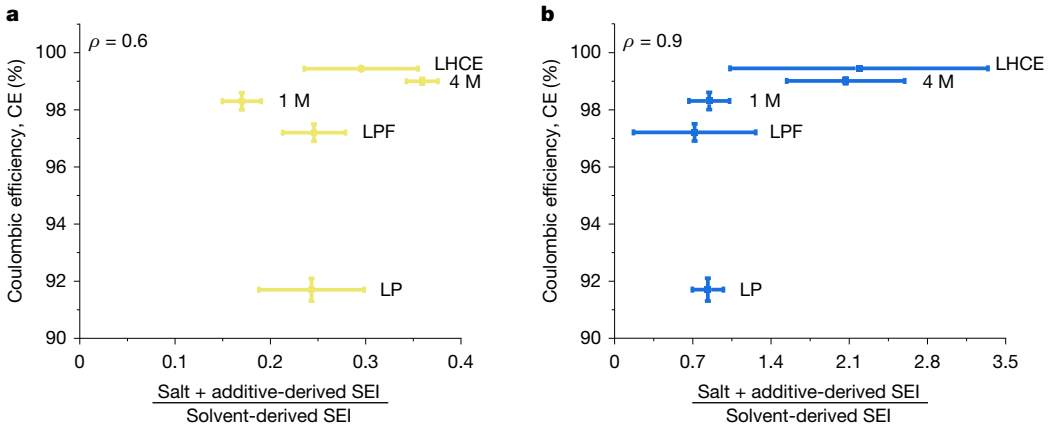

Fig. 4 | Correlation between relative salt- and additive-derived SEI content and CE across diverse electrolyte chemistries. a,**b**, CE (Supplementary Table 2) from Aurbach's method[15,46] in relation to relative salt and fluorinated additive-derived content of SEI from RT-XPS (**a**) and cryo-XPS (**b**). (Salt + additive-derived SEI)/Solvent-derived SEI indicates (F + S + N)/C in LiFSI-based and (F + P)/C in $LiPF_6$-based electrolytes. The measurements are carried out in 1 M $LiPF_6$/EC-DEC (LP), 90 vol% 1 M $LiPF_6$/EC-DEC with 10 vol% FEC (LPF), 1 M LiFSI/DME (1 M), 4 M LiFSI/DME (4 M) and LiFSI-1.2 DME-3 TTE by molar ratio (LHCE) electrolytes. The error bars of XPS results are calculated from the analysis of three different spots of the same sample. Spearman's rank correlation coefficient[41] (ρ) is calculated from the average values of the CE and relative salt- and additive-derived content.

effect is minor. Next, we assess the relative impact of beam damage decoupled from reaction and UHV effects by comparing the composition change between cryo-XPS and the first RT-XPS spectra (Fig. 3e). We find that the LiF intensity difference observed between cryo-XPS and the first RT-XPS spectra is much higher than that between the first and the fifth RT-XPS spectra. This result indicates that the reaction and UHV effects can cause major composition evolution during XPS analysis of sensitive SEI samples. Moreover, beam damage is only a minor effect during cryo-XPS, causing slight composition evolution, which does not occur until the fourth consecutive spectrum (Fig. 3d). Furthermore, SEI spectra are generally not collected from the same spot multiple times in a row, so the practical spectra collection can be considered free from any substantial beam damage effect. The reactions towards a slight increase in LiF content from beam damage may be due to primary photoelectron or secondary electron attack, resulting in the defluorination of C-F/SO_xF_y species[14]. Additional beam effect data are provided in Supplementary Fig. 4. This observed negligible effect of the X-ray beam in XPS is unlike TEM, in which electron beam damage to lithium is found to be an important effect, motivating cryo-TEM[12]. This difference is because a low-energy X-ray beam (about 1.5 keV) is used in our XPS analysis, whereas TEM requires a high-energy electron beam (around 80–300 keV) and a very thin ($\lesssim$100 nm) electron-transparent sample, making it more susceptible to beam damage[36,37]. Nonetheless, the extent of beam damage may vary depending on the X-ray source and setup.

Correlation of SEI composition with performance

Because cryo-XPS provides information on the pristine SEI with preservation, we use it to correlate SEI composition and CE. We measure salt- and additive-derived SEI over solvent-derived SEI from XPS for different electrolyte chemistries. For $LiPF_6$ salt-based carbonate electrolytes and for LiFSI salt-based ether electrolytes, the (F + P)/C ratio and (F + S + N)/C ratio are used, respectively. The proposed ratios are rational because salt and additive-derived SEI measure the relative total inorganic or beneficial content in the SEI[29,30,38–40]. We calculate the Spearman coefficient[41] (ρ) to measure the strength and direction of the monotonic relationship between ranked SEI composition and CE. Although the correlation is only moderate with regular RT-XPS (ρ = 0.6; Fig. 4a), a highly positive correlation is observed with cryo-XPS (ρ = 0.9; Fig. 4b). Moreover, our data show that the trend applies to cycled SEI, or residual SEI studies, in which we observe a relatively higher salt-derived residual SEI for the high-performing 4 M electrolyte compared with the low-performing LP electrolyte (Supplementary Fig. 5). We also study F/C and CE correlation to understand the impact of fluorinated species[30,42,43]. In line with the proposed benefits of fluorinated species in existing literature towards high CE[27,42,44], the F/C correlation is found to be positive with cryo-XPS (ρ = 0.6; Extended Data Fig. 10). Counterintuitively, a negative moderate correlation is observed with RT-XPS (ρ = −0.6), suggesting that RT-XPS is potentially ineffective in providing a rational correlation across diverse electrolyte chemistries. Moreover, we observe larger calculated ratios and larger error bars with cryo-XPS. The error bars further increase in size with additive-based LPF and LHCE. The significant deviation in the ratio values with cryo-XPS and RT-XPS is due to a combination of complex RT reactions and the UHV effect. Based on previous discussions on reaction effect (Fig. 3a) and sputtering (Extended Data Fig. 9), we speculate that only stable species dominate the composition during RT-XPS, resulting in lower heterogeneity (Fig. 4a and Extended Data Fig. 10a). By contrast, the larger error bars with cryo-XPS (Fig. 4b and Extended Data Fig. 10b) are associated with the co-existence of both stable and unstable SEI species at cryoT, resulting in a more heterogeneous composition. The higher heterogeneity of the pristine SEI composition found with cryo-XPS can be further rationalized, knowing that the SEI is inherently heterogeneous[6,7,45]. The results overall indicate that cryo-XPS can provide improved, performance-based correlations across different electrolyte chemistries.

Our description of the pristine SEI from cryo-XPS avoids previous limitations of irreversible chemical compositional evolution of the SEI and volatilization of species under UHV. Moreover, from the pristine SEI chemical composition obtained through cryo-XPS, we find a significant positive correlation between the inorganic-rich SEI content and CE across different electrolyte classes. Although our results challenge existing analyses of the SEI based on characterization with RT-XPS, we view this as an opportunity to redefine our understanding and provide a more reliable interpretation of the pristine SEI speciation. By providing a more precise chemical understanding of the SEI in its pristine form, we anticipate that our study will accelerate the improvement of Li metal batteries. Most importantly, we expect our research to inspire future studies of sensitive and reactive interface characterization under cryogenic conditions to ensure pristine state preservation.

Online content

Any methods, additional references, Nature Portfolio reporting summaries, source data, extended data, supplementary information,

acknowledgements, peer review information; details of author contributions and competing interests; and statements of data and code availability are available at https://doi.org/10.1038/s41586-025-09618-3.

1. Oyakhire, S. T., Gong, H., Cui, Y., Bao, Z. & Bent, S. F. An X-ray photoelectron spectroscopy primer for solid electrolyte interphase characterization in lithium metal anodes. *ACS Energy Lett.* **7**, 2540–2546 (2022).
2. Yu, W., Yu, Z., Cui, Y. & Bao, Z. Degradation and speciation of Li salts during XPS analysis for battery research. *ACS Energy Lett.* **7**, 3270–3275 (2022).
3. Bard, A. J. et al. ChemInform Abstract: the electrode/electrolyte interface - a status report. *J. Phys. Chem.* **97**, 7147–7173 (1993).
4. Yu, X. & Manthiram, A. Electrode-electrolyte interfaces in lithium-based batteries. *Energy Environ. Sci.* **11**, 527–543 (2018).
5. Stamenkovic, V. R., Strmcnik, D., Lopes, P. P. & Markovic, N. M. Energy and fuels from electrochemical interfaces. *Nat. Mater.* **16**, 57–69 (2017).
6. Lin, D., Liu, Y. & Cui, Y. Reviving the lithium metal anode for high-energy batteries. *Nat. Nanotechnol.* **12**, 194–206 (2017).
7. Li, Y., Leung, K. & Qi, Y. Computational exploration of the Li-electrode|electrolyte interface in the presence of a nanometer thick solid-electrolyte interphase layer. *Acc. Chem. Res.* **49**, 2363–2370 (2016).
8. Winter, M. The solid electrolyte interphase – the most important and the least understood solid electrolyte in rechargeable Li batteries. *Z. Phys. Chem.* **223**, 1395–1406 (2009).
9. Dedryvère, R. et al. XPS identification of the organic and inorganic components of the electrode/electrolyte interface formed on a metallic cathode. *J. Electrochem. Soc.* **152**, A689 (2005).
10. Kanamura, K., Tamura, H., Shiraishi, S. & Takehara, Z.-I. XPS analysis for the lithium surface immersed in γ-butyrolactone containing various salts. *J. Electrochem. Soc.* **40**, 913–921 (1995).
11. Andersson, A. M. & Edström, K. Chemical composition and morphology of the elevated temperature SEI on graphite. *J. Electrochem. Soc.* **148**, A1100 (2001).
12. Li, Y. et al. Atomic structure of sensitive battery materials and interfaces revealed by cryo-electron microscopy. *Science* **358**, 506–510 (2017).
13. Boyle, D. T. et al. Corrosion of lithium metal anodes during calendar ageing and its microscopic origins. *Nat. Energy* **6**, 487–494 (2021).
14. Steinrück, H. G. et al. Interfacial speciation determines interfacial chemistry: X-ray-induced lithium fluoride formation from water-in-salt electrolytes on solid surfaces. *Angew. Chem. Int. Ed.* **59**, 23180–23187 (2020).
15. Zhang, Z. et al. Capturing the swelling of solid-electrolyte interphase in lithium metal batteries. *Science* **375**, 66–70 (2022).
16. Wang, X. et al. New insights on the structure of electrochemically deposited lithium metal and its solid electrolyte interphases via cryogenic TEM. *Nano Lett.* **17**, 7606–7612 (2017).
17. Zachman, M. J., Tu, Z., Choudhury, S., Archer, L. A. & Kourkoutis, L. F. Cryo-STEM mapping of solid–liquid interfaces and dendrites in lithium-metal batteries. *Nature* **560**, 345–349 (2018).
18. Zhang, Z. et al. Cryogenic electron microscopy for energy materials. *Acc. Chem. Res.* **54**, 3505–3517 (2021).
19. Bai, X., McMullan, G. & Scheres, S. H. W. How cryo-EM is revolutionizing structural biology. *Trends Biochem. Sci* **40**, 49–57 (2015).
20. Dubochet, J. On the development of electron cryo-microscopy (Nobel Lecture). *Angew. Chem. Int. Ed.* **130**, 10842–10846 (2018).
21. Henderson, R. From electron crystallography to single particle CryoEM (Nobel Lecture). *Angew. Chem. Int. Ed.* **130**, 10804–10825 (2018).
22. Taylor, K. A. & Glaeser, R. M. Electron diffraction of frozen, hydrated protein crystals. *Science* **186**, 1036–1037 (1974).
23. McDowall, A. W. et al. Electron microscopy of frozen hydrated sections of vitreous ice and vitrified biological samples. *J. Microsc.* **131**, 1–9 (1983).
24. Henderson, R., Baldwin, J. M., Downing, K. H., Lepault, J. & Zemlin, F. Structure of purple membrane from *Halobacterium halobium*: recording, measurement and evaluation of electron micrographs at 3.5 Å resolution. *Ultramicroscopy* **19**, 147–178 (1986).
25. Fernandez-Moran, H. Cell-membrane ultrastructure: low-temperature electron microscopy and X-ray diffraction studies of lipoprotein components in lamellar systems. *Circulation* **26**, 1039–1065 (1962).
26. Tan, J., Matz, J., Dong, P., Shen, J. & Ye, M. A. A growing appreciation for the role of LiF in the solid electrolyte interphase. *Adv. Energy Mater.* **11**, 2100046 (2021).
27. Li, T., Zhang, X.-Q., Shi, P. & Zhang, Q. Fluorinated solid-electrolyte interphase in high-voltage lithium metal batteries. *Joule* **3**, 2647–2661 (2019).
28. Wang, C., Meng, Y. S. & Xu, K. Perspective—fluorinating Interphases. *J. Electrochem. Soc.* **166**, A5184–A5186 (2019).
29. Hobold, G. M., Wang, C., Steinberg, K., Li, Y. & Gallant, B. M. High lithium oxide prevalence in the lithium solid–electrolyte interphase for high Coulombic efficiency. *Nat. Energy* **9**, 580–591 (2024).
30. Kim, M. S. et al. Suspension electrolyte with modified Li+ solvation environment for lithium metal batteries. *Nat. Mater.* **21**, 445–454 (2022).
31. Lin, D. et al. Fast galvanic lithium corrosion involving a Kirkendall-type mechanism. *Nat. Chem.* **11**, 382–389 (2019).
32. Arkel, A. E., Spitsbergen, U. & Heyding, R. D. Note on the volatility of lithium oxide. *Can. J. Chem.* **33**, 446–447 (1955).
33. Kudo, H., Wu, C. H. & Ihle, H. R. Mass-spectrometric study of the vaporization of Li_2O(s) and thermochemistry of gaseous LiO, Li_2O, Li_3O, and Li_2O_2. *J. Nucl. Mater.* **78**, 380–389 (1978).
34. Seah, M. P. & Dench, W. A. Quantitative electron spectroscopy of surfaces: a standard data base for electron inelastic mean free paths in solids. *Surf. Interface Anal.* **1**, 2–11 (1979).
35. D'Acunto, G. et al. Atomic layer deposition of hafnium oxide on InAs: insight from time-resolved *in situ* studies. *ACS Appl. Electron Mater* **2**, 3915–3922 (2020).
36. Walther, T. in *Microscopy Methods in Nanomaterials Characterization* 105–134 (Elsevier, 2017).
37. García De Abajo, F. J. & Di Giulio, V. Optical excitations with electron beams: challenges and opportunities. *ACS Photon.* **8**, 945–974 (2021).
38. Jagger, B. & Pasta, M. Solid electrolyte interphases in lithium metal batteries. *Joule* **7**, 2228–2244 (2023).
39. He, M., Guo, R., Hobold, G. M., Gao, H. & Gallant, B. M. The intrinsic behavior of lithium fluoride in solid electrolyte interphases on lithium. *Proc. Natl Acad. Sci. USA* **117**, 73–79 (2019).
40. Kim, M. S. et al. Revealing the multifunctions of Li_3N in the suspension electrolyte for lithium metal batteries. *ACS Nano* **17**, 3168–3180 (2023).
41. Spearman, C. The proof and measurement of association between two things. *Am. J. Psychol.* **15**, 72–101 (1904).
42. Oyakhire, S. T. et al. Proximity matters: interfacial solvation dictates solid electrolyte interphase composition. *Nano Lett.* **23**, 7524–7531 (2023).
43. Oyakhire, S. T. & Bent, S. F. Interfacial engineering of lithium metal anodes: what is left to uncover? *Energy Adv.* **3**, 108–122 (2023).
44. Yu, Z. et al. Rational solvent molecule tuning for high-performance lithium metal battery electrolytes. *Nat. Energy* **7**, 94–106 (2022).
45. Peled, E., Golodnitsky, D. & Ardel, G. Advanced model for solid electrolyte interphase electrodes in liquid and polymer electrolytes. *J. Electrochem. Soc.* **144**, L208 (1997).
46. Cui, Z. et al. Molecular anchoring of free solvents for high-voltage and high-safety lithium metal batteries. *Nat. Commun.* **15**, 2033 (2024).

Publisher's note Springer Nature remains neutral with regard to jurisdictional claims in published maps and institutional affiliations.

Springer Nature or its licensor (e.g. a society or other partner) holds exclusive rights to this article under a publishing agreement with the author(s) or other rightsholder(s); author self-archiving of the accepted manuscript version of this article is solely governed by the terms of such publishing agreement and applicable law.

© The Author(s), under exclusive licence to Springer Nature Limited 2025

Methods

Materials

All electrolytes were prepared and handled in an argon-filled glovebox with an O_2 concentration of <0.1 ppm and H_2O concentration of <0.01 ppm. Lithium bis(fluorosulfonyl)imide or LiFSI (Fluolyte) was used as a salt. 1,2-Dimethoxyethane or DME (Sigma-Aldrich) and diethyl carbonate or DEC (Sigma-Aldrich) were used as solvents. 1,1,2,2-Tetrafluoroethyl 2,2,3,3-tetrafluoropropylether or TTE (SynQuest) was used as a diluent in LHCE electrolyte. Lithium hexafluorophosphate or $LiPF_6$ (1 M) in EC/DEC (LP) and fluoroethylene carbonate or FEC were purchased from Gotion. The electrolyte formulations used were 1 M $LiPF_6$/EC-DEC (LP), 90 vol% 1 M $LiPF_6$/EC-DEC with 10 vol% FEC (LPF), 1 M LiFSI/DME (1 M), 4 M LiFSI/DME (4 M) and LiFSI-1.2 DME-3 TTE by molar ratio (LHCE) (Supplementary Table 2). The commercial Li battery separator Celgard 2325 (25 µm thick, polypropylene/polyethylene/polypropylene or PP/PE/PP) was purchased from Celgard. CR2032-type coin cells were used for all experiments. Thick Li foil (about 750 µm thick) and Cu current collector (25 µm thick Cu foil) were purchased from Alfa Aesar.

Electrochemical measurement

All electrochemical measurements were performed using an Arbin battery cycler with Li|Cu coin cells. All cells were prepared inside an argon-filled glovebox. Li was mechanically scraped with a polyethylene scraper to remove the surface oxide and improve the electrical connection. Electrolytes (60 µl) were used in all the coin cells. The coin cells were transferred to the glovebox for sample preparation immediately after the electrochemical tests. For SEI characterization on top of electrodeposited lithium, a plating capacity of 0.5 mAh cm^{-2} and a current density of 1 mA cm^{-2} were used for all XPS experiments. For SEI characterization on top of the Cu current collector before Li electrodeposition (Extended Data Fig. 5), a 10 mV compared with Li/Li^+ potential hold was applied on Cu for 30 min.

Materials characterization

The cryo-XPS transfer protocol is shown in Fig. 1. The Versa Probe III, IV XPS instrument (PHI) available at Stanford Nano Shared Facilities was used for all the XPS experiments. Unless otherwise mentioned, 60 µl of respective solvent (DEC for LP and LPF, and DME for 1 M, 4 M and LHCE) was used after cell disassembly for rinsing the electroplated Li^0 on Cu current collector. Rinsing with 60 µl solvent is a commonly used process in literature for removing residual electrolyte[30,47]. A manual hand blower was used for drying the SEI quickly (about 4–8 s) inside the glovebox. A quick drying process was chosen so that the sample could be frozen and the spontaneous RT reactions could be halted as soon as possible. For the specific cases of unwashed SEI, the sample was kept unwashed, and around 3–5 s of manual one-sided blotting was performed using a filter paper (Whatman 42.5 mm diameter) and a tweezer adapted from ref. 15 to remove the excess electrolyte. The drying time and blotting time slightly varied for different electrolytes, and human judgement was used to ensure completion (no visible signs of liquid or wetness). A regular rinsing and drying process that is typically employed for SEI samples during XPS is used so that the sample preparation protocol does not induce any changes[30,47]. The Cu current collector was cut into half to reduce pumping time. The samples were then placed inside a sealed Eppendorf tube and taken out from the glovebox to immediately perform plunge freezing by breaking the tube with pliers in liquid N_2 (about −196 °C) without any air exposure. Then, the samples were transferred to XPS using a larger liquid N_2 dewar that contained the cryogenic sample storage vial, which takes around 5–10 min. For longer duration of storage, frequent refilling of the LN_2 cylinder and additional preservation effect studies may be needed. The cryo-XPS sample holder was precooled to −110 °C (minimum allowed temperature) before loading the cryogenic samples into the intro chamber to maintain the cryo conditions of the sample. The cryogenic sample holder was a specialized sample holder with a cold finger connected through stage control for in situ cooling. The N_2 pressure, higher than ambient pressure, inside the intro chamber ensured an inert environment around the sample to preserve it from air and moisture right before pumping. Owing to the fast-pumping process of the instrument (about 5–10 min) and the precooled sample holder, the samples maintained cryoT. About 10 min of pumping results in a sample temperature of about −110 °C as estimated from the reading of a thermocouple placed on the holder in the main chamber. A continuous supply of liquid N_2 was provided to the cold finger, and a PID controller was used to maintain a temperature of about −110 °C in the main chamber. The spectral collection was also performed at around −110 °C during cryo-XPS.

For cryo-heated to RT-XPS (about 25 °C), the PID controller set parameters were optimized to prevent any sudden temperature spikes above RT, and the same parameters were used for all the samples to ensure a comparable heating rate (refer to Supplementary Table 3 for the values of PID controller parameters). The heating process took around 8.5 min from −110 °C to 25 °C (set point). We also consider the effect of evaporation time and related SEI composition changes (refer to Supplementary Note 7 and Supplementary Fig. 6 for further details; and Supplementary Note 8 for discussion on SEI stability during plunge freezing and thawing). For RT-XPS, after sample preparation, the samples were transferred from the argon-filled glovebox to the XPS chamber using a sealed vessel, and experiments were performed using regular sample holders.

The XPS measurements performed in the Versa Probe III, IV XPS instrument (PHI) uses a monochromatic Al–Kα source at 1,486.6 eV. In the built-in conditions of the instrument, the angle between the analyser and sample holder is 45°, which was used during all the experiments (for further details on photoelectron escape depth, see Supplementary Note 6). A precise *z*-height calibration was ensured before spectra collection to maximize the photoelectron signal. High-resolution scans were collected using a 55 eV pass energy, 0.81 eV energy resolution, 20 ms dwell time and 0.1 eV step size. Survey scans were collected using a 224 eV pass energy, 1.40 eV energy resolution, 20 ms dwell time and 0.8 eV step size. For Ar^+ sputtering, a 1 kV, 0.7 µA and 2 × 2 mm gun setting was used for 30 s at an angle of 33° to the sample holder. Owing to the poor electrical conductivity of the SEI, electron and ion neutralizers (E-neut, I-neut) were used during spectra collection. The negligible changes between cryo 0 min and cryo 60 min spectra (Fig. 2 and Extended Data Figs. 1 and 3), between consecutive spectra (Fig. 3d,e) to study beam damage, and between spectra collected without and with E-neut and I-neut (Supplementary Figs. 7 and 8) support negligible damage in the presence of dual electron and ion neutralizers. Note further that only the independent use of an electron neutralizer may result in Li metal formation, based on the literature[48]. Please refer to ref. 49 for more details on using charge neutralization and ref. 15 for cryo-TEM and cryo-STEM EELS measurements and sample preparation.

Supplementary Note 9 and Supplementary Fig. 9 provide a discussion on cathode electrolyte interphase (CEI) characterization using cryo-XPS. Lithium nickel manganese cobalt oxide or NMC 811 (MSE Supplies), C65 carbon black and polyacryic acid (PAA) binder were mixed in 84:8:8 (wt:wt:wt) ratio in 1-methyl-2-pyrrolidone (NMP) solution. A slurry was mixed with a Thinky mixer and was coated on the Al foil. After drying at 70 °C in a vacuum oven for 30 h, we fabricated 50 µm Li ||NMC 811 and cycled it 10 times using 2 M LiFSI in 2-[2-(2,2-difluoroethoxy)ethoxy]-1,1,1-trifluoroethane or F5DEE using C/2 charge 1 C discharge rates.

All XPS data were analysed using the Multipak software (PHI). We used LiF-based[2] spectral calibration, as C 1*s*-based calibration may lead to misinterpretations[50]. The LiF peak position was fixed at 684.5 eV, consistent with the literature[51,52]. For every spectrum, the relative positions of all the peaks were checked to ensure the calibration was correct.

The peaks were assigned based on several publications[1,30,42,53–55] with human judgement, and LiF-based relative shifting was applied to the referenced articles to ensure peak position accuracy. Note that the IUPAC-recommended definition for chemical speciation is used in the interpretation of the data, which includes both identification and quantitative differences of different molecular and atomic species[56,57]. For normalization with respect to the C–F/SO_xF_y peak, a specific binding energy position at about 687.5 eV is chosen for accuracy. Further accuracy in the SO_xF_y/C–F peak position is also ensured by comparing its relative peak position with respect to the LiF peak. SO_xF_y/C–F-based normalization helps to easily visualize the ongoing phenomenon in agreement with the literature, which also shows an increase in LiF species[1,2]. Global normalization based on a singular species helps us to understand the relative amounts of different species when multiple spectra are compared.

Data availability

All data needed to evaluate the conclusions are present in the paper or the Supplementary Information. Source data are provided with this paper.

47. Zhang, W. et al. Recovery of isolated lithium through discharged state calendar ageing. *Nature* **626**, 306–312 (2024).
48. Otto, S.-K. et al. In-depth characterization of lithium-metal surfaces with XPS and ToF-SIMS: toward better understanding of the passivation layer. *Chem. Mater.* **33**, 859–867 (2021).
49. Baer, D. R. XPS guide: charge neutralization and binding energy referencing for insulating samples. *J. Vac. Sci. Technol. A* **38**, 031204 (2020).
50. Greczynski, G. & Hultman, L. Compromising science by ignorant instrument calibration—need to revisit half a century of published XPS data. *Angew. Chem. Int. Ed.* **59**, 5002–5006 (2020).
51. Liu, Q. et al. A fluorinated cation introduces new interphasial chemistries to enable high-voltage lithium metal batteries. *Nat. Commun.* **14**, 3678 (2023).
52. Ge, S. et al. High safety and cycling stability of ultrahigh energy lithium ion batteries. *Cell Rep. Phys. Sci.* **2**, 100584 (2021).
53. Wood, K. N. & Teeter, G. XPS on Li-battery-related compounds: analysis of inorganic SEI phases and a methodology for charge correction. *ACS Appl. Energy Mater.* **1**, 4493–4504 (2018).
54. Rustomji, C. S. et al. Liquefied gas electrolytes for electrochemical energy storage devices. *Science* **356**, eaal4263 (2017).
55. Ren, X. et al. Enabling high-voltage lithium-metal batteries under practical conditions. *Joule* **3**, 1662–1676 (2019).
56. Templeton, D. M. et al. Guidelines for terms related to chemical speciation and fractionation of elements. Definitions, structural aspects, and methodological approaches (IUPAC recommendations 2000). *Pure Appl. Chem.* **72**, 1453–1470 (2009).
57. Feldmann, J. et al. Microwave-assisted sample preparation for element speciation. in *Microwave-Assisted Sample Preparation for Trace Element Determination* 281–312 (Elsevier, 2014).
58. Greczynski, G. & Hultman, L. Towards reliable X-ray photoelectron spectroscopy: sputter-damage effects in transition metal borides, carbides, nitrides, and oxides. *Appl. Surf. Sci.* **542**, 148599 (2021).

Acknowledgements S.B.S. acknowledges support from the TomKat Center Graduate Fellowship for Translational Research and the Link Foundation Energy Fellowship. G.D.A. acknowledges support from the Wallenberg Foundation Postdoctoral Scholarship Program. S.T.O. acknowledges support from the Schmidt Science Postdoctoral Fellowship. K.M.S.G. acknowledges support from NSF GRFP. Y.C. acknowledges the cryo-EM research support from the Department of Energy, Office of Basic Energy Sciences, Division of Materials Science and Engineering under contract DE-AC02-76SF00515, and the support from Assistant Secretary for Energy Efficiency and Renewable Energy, Office of Vehicle Technologies, of the US Department of Energy under the Battery Materials Research Program, the Battery500 Consortium program, and the CEI consortium program. S.F.B. acknowledges support from the Stanford StorageX initiative seed grant award. Part of this work was performed at the Stanford Nano Shared Facilities supported by the National Science Foundation under award no. ECCS-2026822. S.B.S. acknowledges the discussions with J. Lee and W. Zhang on cryo-XPS transfer. S.B.S. appreciates D. Li and J.H. Lee for providing the LHCE electrolyte.

Author contributions S.B.S., S.F.B. and Y.C. conceived the idea and designed experiments. S.B.S. performed all the electrochemical experiments and conducted all the RT-XPS and cryo-XPS experiments. S.B.S. and G.D. developed the cryo-XPS transfer process. G.D. assisted with cryo-XPS experiments during the initial phase of the study. P.S. and S.T.O. assisted with experimental designs. K.M.S.G. assisted with data interpretation discussions and manuscript editing. J.R.-J. helped with cryo-XPS transfer development and instrument-related discussions. S.B.S. analysed and interpreted the data with assistance and feedback from all the authors. S.B.S. wrote the first draft of the manuscript, which was edited and revised by all the authors. I.R.C. assisted with electrochemical tests for CEI characterization. S.F.B. and Y.C. supervised the project in all aspects.

Competing interests The authors declare no competing interests.

Additional information

Supplementary information The online version contains supplementary material available at https://doi.org/10.1038/s41586-025-09618-3.

Correspondence and requests for materials should be addressed to Yi Cui or Stacey F. Bent.

Peer review information *Nature* thanks Zhouguang Lu and the other, anonymous, reviewer(s) for their contribution to the peer review of this work. Peer reviewer reports are available.

Reprints and permissions information is available at http://www.nature.com/reprints.

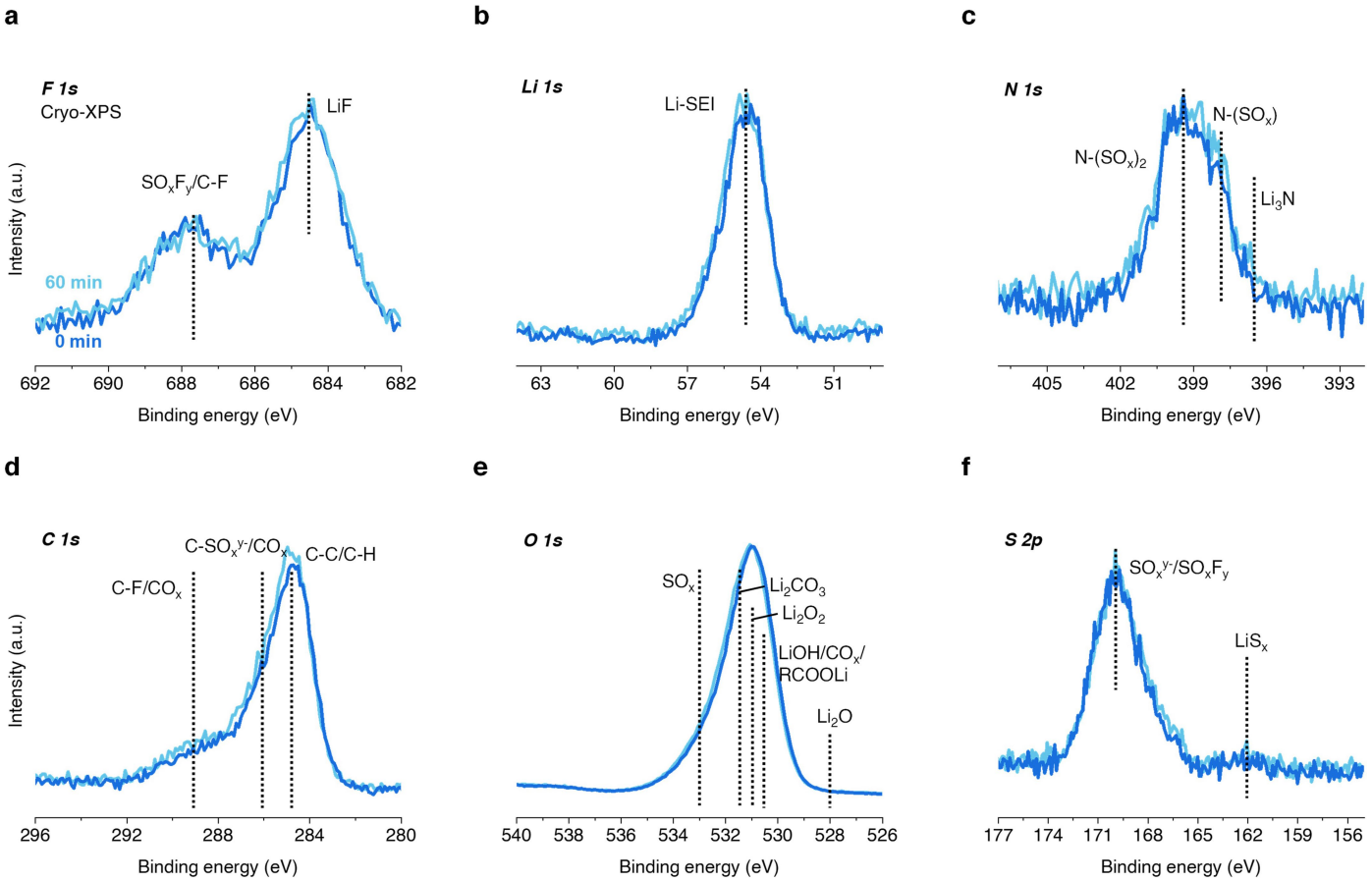

Extended Data Fig. 1 | Time-resolved high-resolution spectra for SEI with cryo-XPS. a-f, All high-resolution spectra for **(a)** F 1 s, **(b)** Li 1 s, **(c)** N 1 s, **(d)** C 1 s, **(e)** O 1 s, **(f)** S 2p with cryo-XPS at 0 min and 60 min. The measurements are carried out in 1 M LiFSI/DME (1 M) electrolyte. Global normalization of all the peaks is performed with respect to the C-F/SO_xF_y peak in F 1 s high-resolution spectra in **(a)**. The measurements are performed on one analysis spot to capture the SEI evolution decoupled from spatial heterogeneities in the SEI.

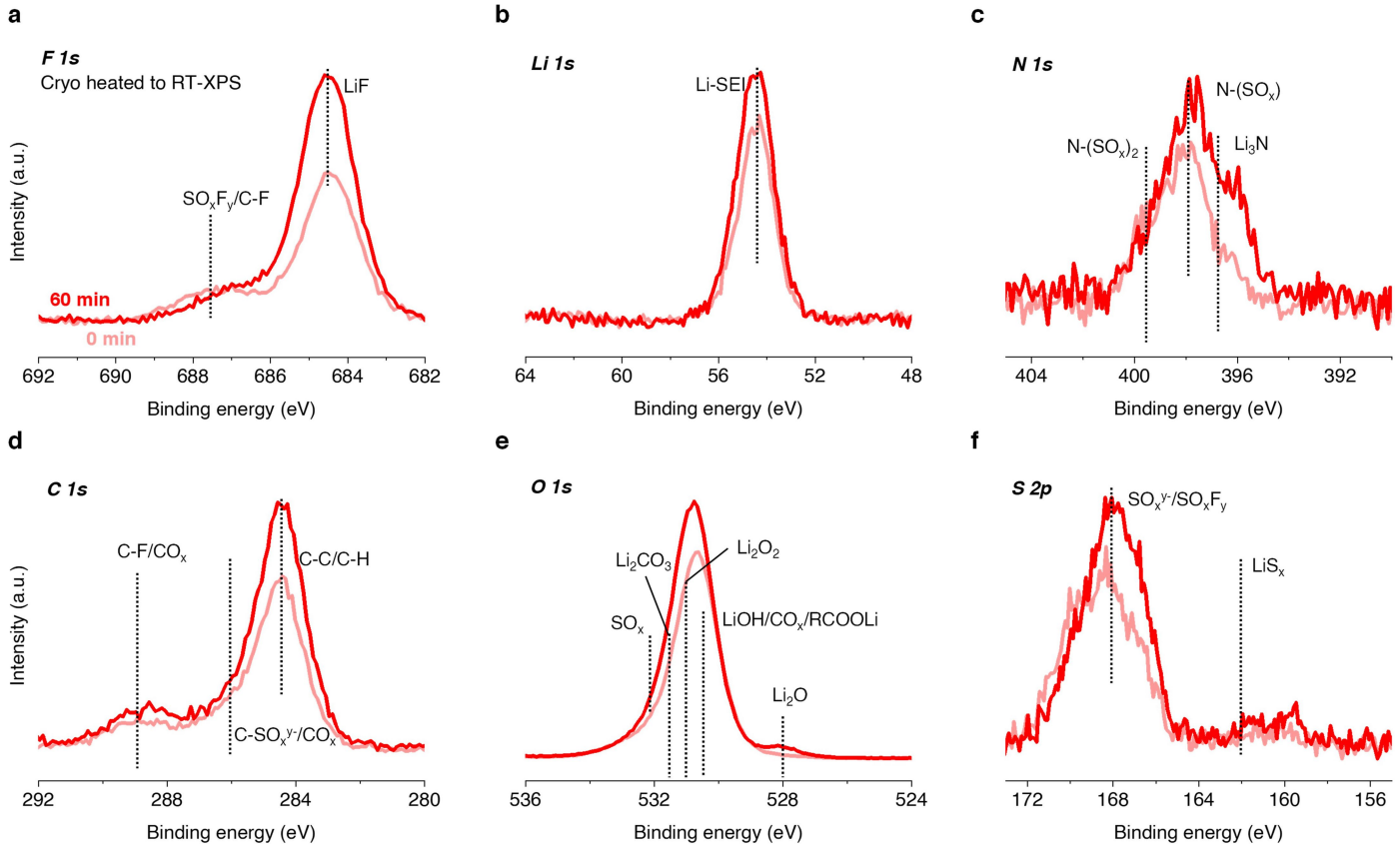

Extended Data Fig. 2 | Time-resolved high-resolution spectra for SEI during cryo heated to RT-XPS. a-f, All high-resolution spectra for **(a)** F 1 s, **(b)** Li 1 s, **(c)** N 1 s, **(d)** C 1 s, **(e)** O 1 s, **(f)** S 2p with cryo heated to RT-XPS at 0 min and 60 min. The measurements are carried out in 1 M LiFSI/DME (1 M) electrolyte. Global normalization of all the peaks is performed with respect to the C-F peak in F 1 s high-resolution spectra in **(a)**. The measurements are performed on one analysis spot to capture the SEI evolution decoupled from spatial heterogeneities in the SEI. The analysis spot is the same as the one shown in Extended Data Fig. 1.

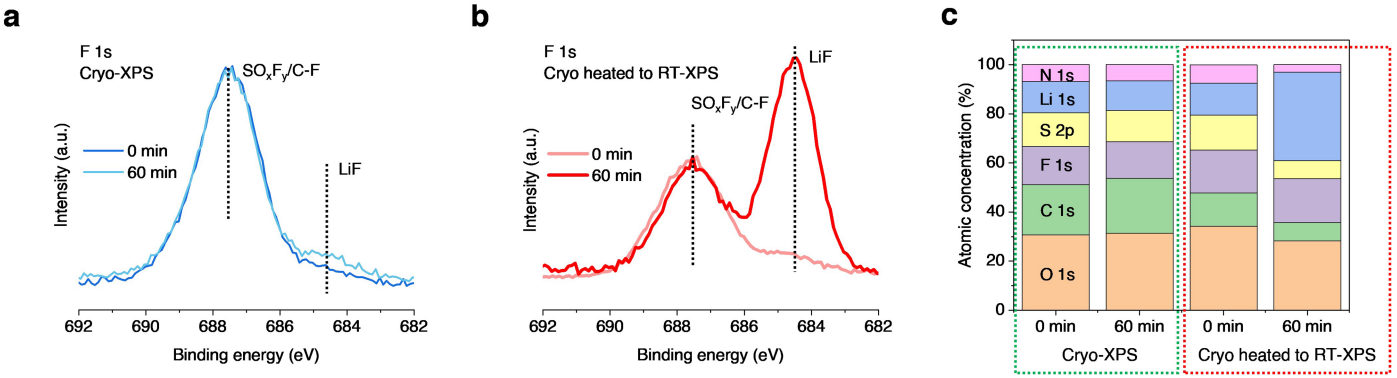

Extended Data Fig. 3 | SEI preservation and evolution effects with cryo-XPS and RT-XPS on unwashed SEI. a-b, High-resolution spectra for F 1 s peaks with **(a)** cryo-XPS and **(b)** cryo heated to RT-XPS at 0 min and at 60 min. **c**, Atomic concentration for unwashed SEI with cryo-XPS and cryo heated to RT-XPS at 0 min and at 60 min. The intensities of F 1 s spectra shown in **(a)** and **(b)** are normalized with respect to the SO_xF_y/ C-F peak. The measurements are performed on one analysis spot to capture the SEI evolution decoupled from spatial heterogeneities in the SEI. The measurements are carried out in 1 M LiFSI/DME (1 M) electrolyte.

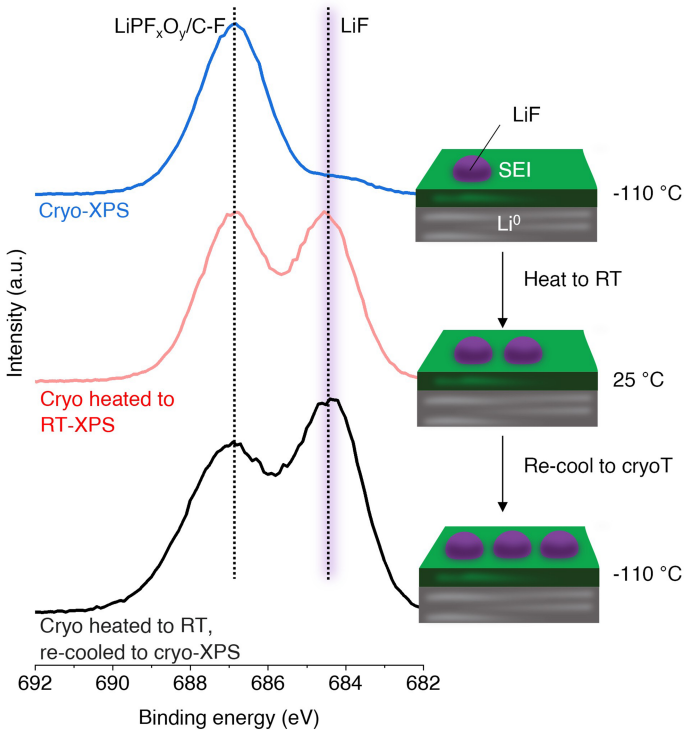

Extended Data Fig. 4 | Effect of gradual re-cooling on SEI preservation. High-resolution F 1 s spectra for with cryo-XPS (blue, top), cryo-heated to RT-XPS (pink, middle), cryo-heated to RT, and then re-cooled to cryo-XPS (black, bottom), respectively. The measurements are performed on one analysis spot to capture the SEI evolution decoupled from spatial heterogeneities in the SEI. The measurements are carried out in 1 M $LiPF_6$/EC-DEC (LP) electrolyte. An unwashed SEI sample is used as the composition is found to be more sensitive to temperature change in Extended Data Fig. 3.

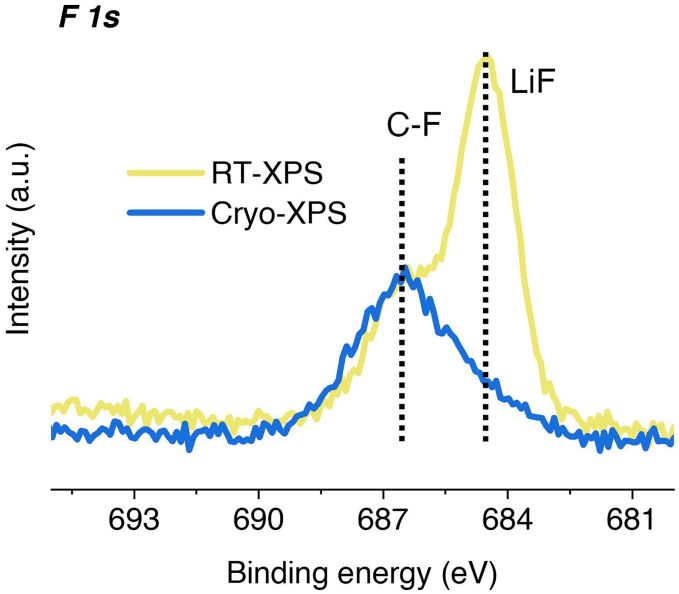

Extended Data Fig. 5 | Effect of cryo-XPS and RT-XPS on the SEI formed on Cu before Li plating. High-resolution spectra for F 1 s peaks of SEI formed on Cu in 1 M $LiPF_6$/EC-DEC (LP) electrolyte using a protocol of holding the Cu current collector at 10 mV above Li electrodeposition potential for 30 min using cryo-XPS and RT-XPS. This protocol ensures no Li is electrodeposited on Cu so that only electrolyte decomposition prior to Li plating can be studied.

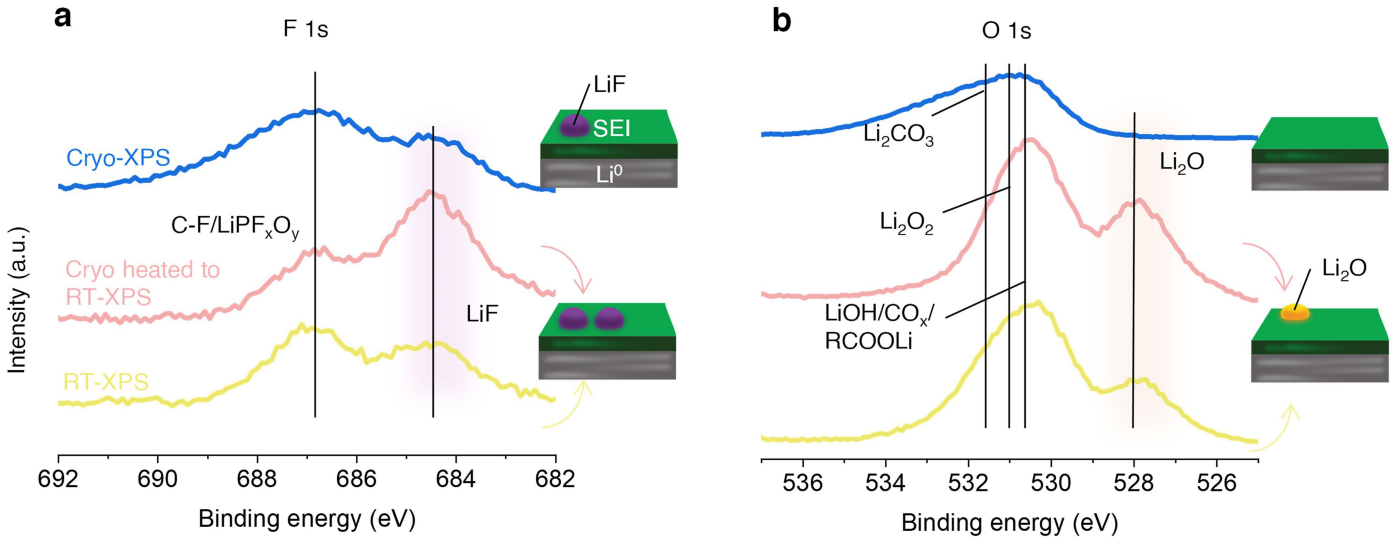

Extended Data Fig. 6 | Reaction effect on SEI chemical composition under cryo-XPS and RT-XPS conditions. a-b, High-resolution spectra for **(a)** F 1 s peaks and **(b)** O 1 s peaks collected using cryo-XPS (blue, top), cryo heated to RT-XPS (pink, middle), and RT-XPS (yellow, bottom) with schematics showing SEI evolution. Global normalization across F 1 s and O 1 s is performed for the same electrolyte with respect to the C-F peak in F 1 s high-resolution spectra shown in **(a)**. The measurements are carried out in 1 M $LiPF_6$/EC-DEC (LP) electrolyte.

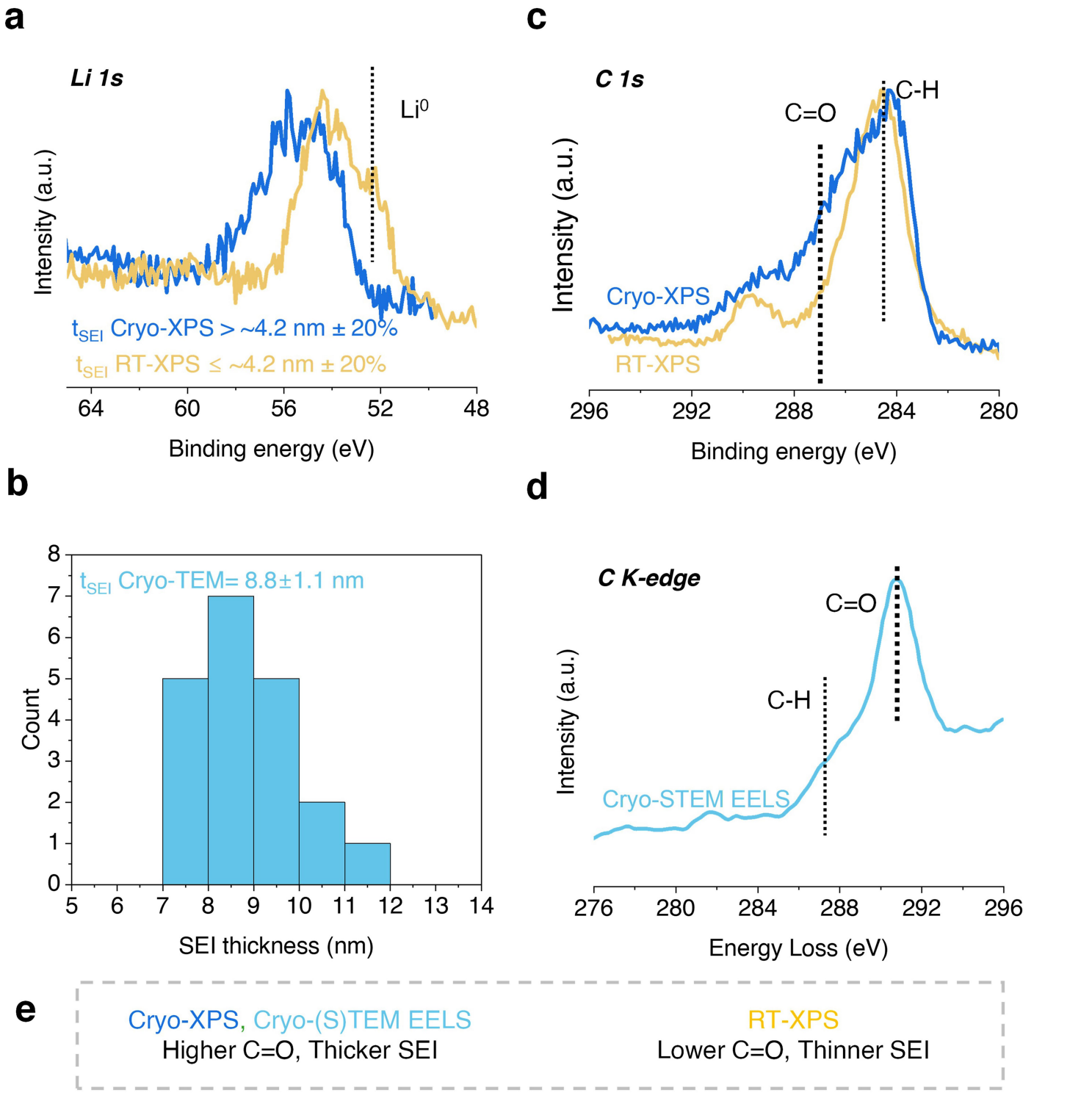

Extended Data Fig. 7 | Cryo-XPS and RT-XPS comparison with cryo-(S)TEM EELS findings. a, c, High-resolution spectra for **(a)** Li 1 s peaks and **(c)** C 1 s peaks with cryo-XPS and RT-XPS. **b**, Histogram showing thickness distribution of the SEI using cryo-TEM. **d**, C K-edge fine structure of Li dendrites using cryo-STEM EELS. **e**, Summary of key findings from cryo-XPS, cryo-STEM EELS and RT-XPS. The intensities of C 1 s and Li 1 s spectra shown in **(a)** and **(c)** are normalized to exhibit the same maximum intensity for both cryo-XPS and RT-XPS data. The measurements in **(a)**-**(d)** are carried out on **(a)**, **(c)** 0.5 mAh cm^{-2} and **(b)**, **(d)** 0.1 mAh cm^{-2} Li deposited on **(a)**, **(c)** Cu foil and **(b)**, **(d)** Cu-evaporated TEM grid at a current density of 1 mA cm^{-2} in 1 M $LiPF_6$/EC-DEC (LP) electrolyte and rinsed by 60 µL DEC. t_{SEI} refers to thickness of the SEI. The data shown in **(b)** and **(d)** are adapted with permission from Zhang, Z. et al., Science, DOI number: 10.1126/science.abi8703 [2022], AAAS[15].

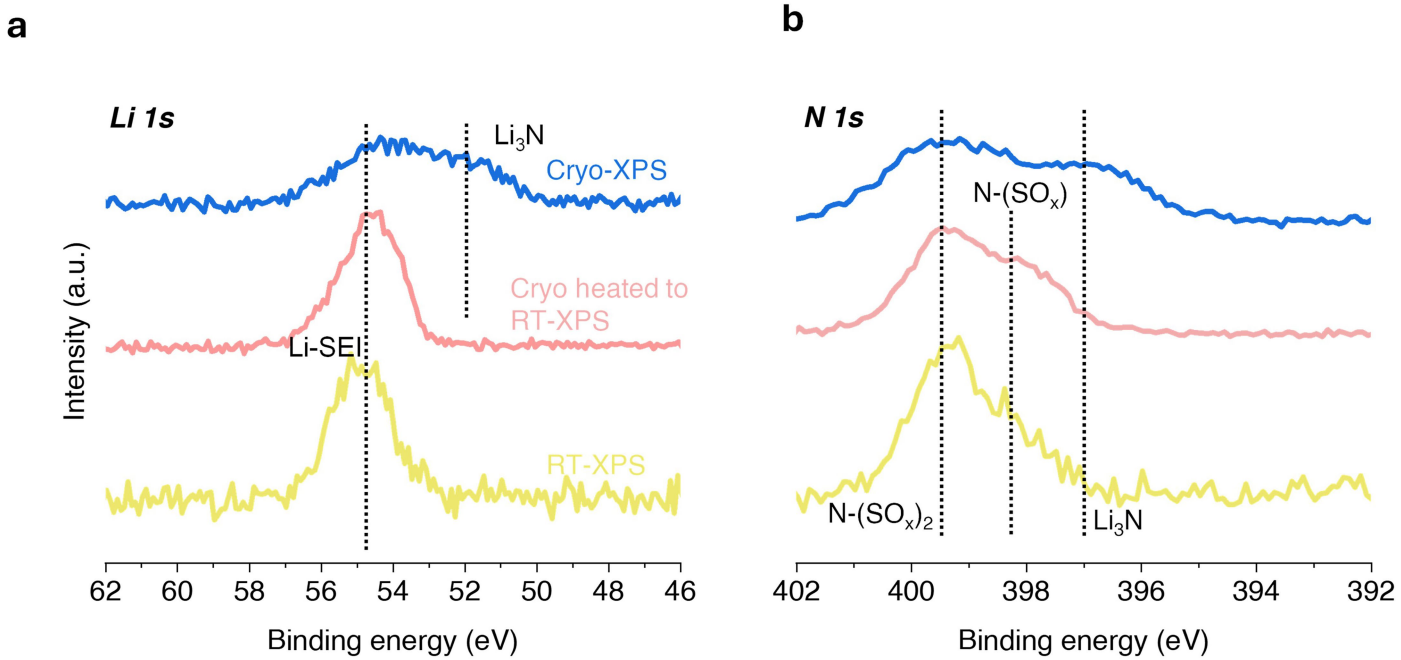

Extended Data Fig. 8 | Temperature-dependent composition evolution effects on SEI species with cryo-XPS and RT-XPS in LHCE-SEI. a-b, High-resolution spectra for **(a)** Li 1 s and **(b)** N 1 s peaks with cryo-XPS (blue, top), cryo heated to RT-XPS (pink, middle), and RT-XPS (yellow, bottom). Global normalization is performed with respect to the C-F peak in F 1 s high-resolution spectra shown in Fig. 3a. The measurements are carried out in LiFSI-1.2 DME-3 TTE by molar ratio (LHCE) electrolyte. We identify the peak near ~52 eV with cryo-XPS as Li_3N (not Li^0 metal) because it appears and disappears in conjunction with the same species peak in N 1 s region. Besides, Li is highly electropositive, so it is more favorable for Li to exist in its compound forms.

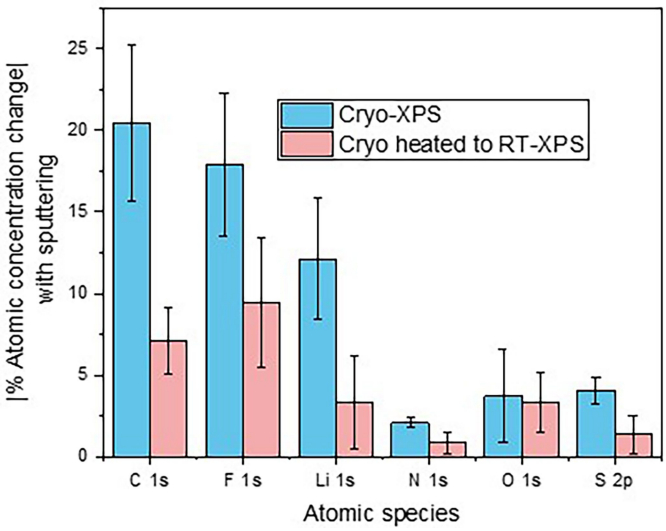

Extended Data Fig. 9 | Effect of Ar^+ ion sputtering on SEI composition during cryo-XPS and RT-XPS. Average % atomic concentration change with sputtering for cryo-XPS and cryo heated to RT-XPS. The measurements are carried out in residual SEI from 4 M LiFSI/DME (4 M) electrolyte after 5 cycles. The error bars of XPS results are calculated from the analysis of three different spots of the same sample. Ar^+ ion sputtering is destructive toward surface chemical composition[1,2,58]. So, the degree of composition change before and after Ar^+ ion sputtering is used to understand the relative amount of stable species in the SEI.

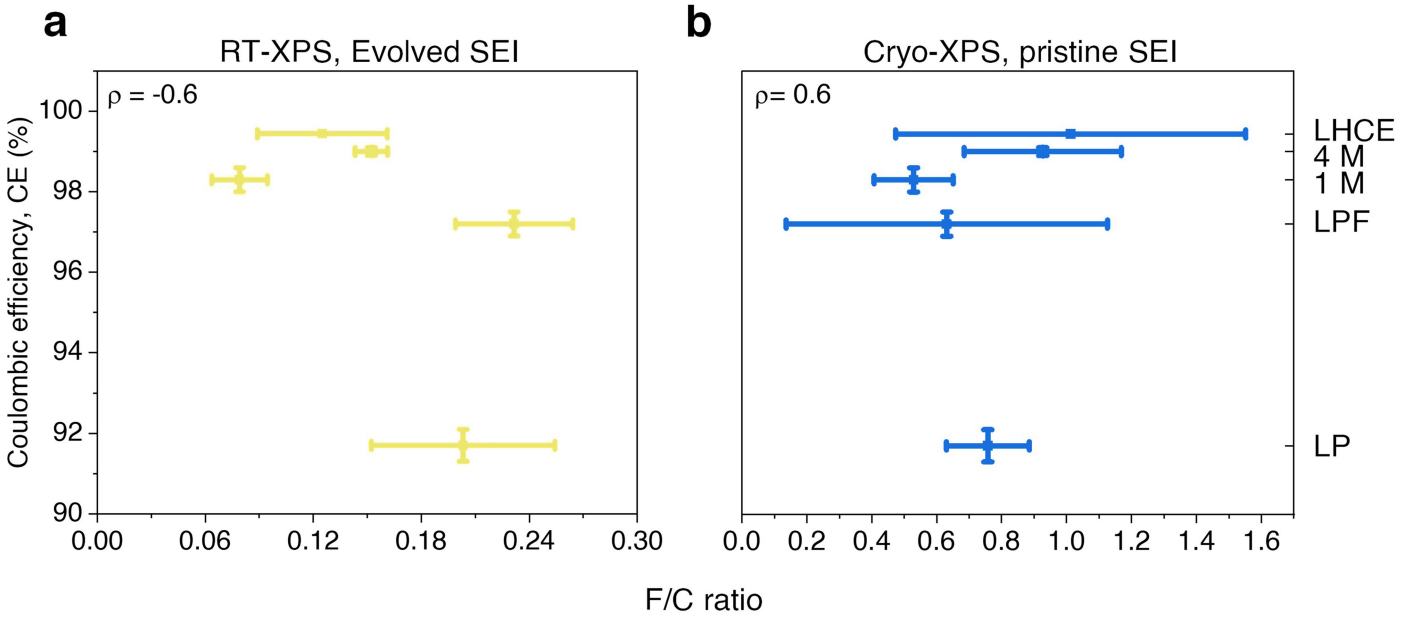

Extended Data Fig. 10 | Correlation between F/C ratio and CE in multiple electrolytes with cryo-XPS and RT-XPS. a-b, CE (Supplementary Table 2) from Aurbach's method[15,46] in relation to the F/C ratio of SEI from **(a)** RT-XPS and **(b)** cryo-XPS. The measurements are carried out on 0.5 mAh cm^{-2} of Li deposited on Cu at a current density of 1 mA cm^{-2} in 1 M $LiPF_6$/EC-DEC (LP), 90 vol% 1 M $LiPF_6$/EC-DEC with 10 vol% FEC (LPF), 1 M LiFSI/DME (1 M), 4 M LiFSI/DME (4 M), and LiFSI-1.2 DME-3 TTE by molar ratio (LHCE) electrolytes. The error bars of XPS results are calculated from the analysis of three different spots of the same sample. Spearman rank correlation coefficient[41] (ρ) is calculated from the average values of the CE and F/C ratio.